BIOPHYSICS

Structural dynamics-guided engineering of a riboswitch RNA for evolving c-di-AMP synthases

Dian Chen[1], Jun Li[2], You Wu[1], Liang Hong[2], Yu Liu[1]*

Cyclic diadenosine monophosphate (C-di-AMP) synthases are key enzymes for synthesizing c-di-AMP, a potent activator of the stimulator of interferon genes (STING) immune pathway. However, characterizing these enzymes has been hampered by the lack of effective sensors. While c-di-AMP riboswitches, as natural aptamers, hold the potential as RNA biosensors, their poorly comprehended structural dynamics and inherent "OFF" genetic output pose substantial challenges. To address these limitations, we synthesized over 10 fluorophore-labeled samples to probe the conformational changes of the riboswitch at the single-molecule level. By integrating these dynamic findings with steady-state fluorescence titration, mutagenesis, in vivo assays, and strand displacement strategy, we transformed the natural aptamer into a c-di-AMP biosensor. This engineered biosensor reversed its genetic output from "OFF" to "ON" upon c-di-AMP binding, exhibiting a 50-fold improvement in the c-di-AMP detection limit. Leveraging this refined biosensor, we developed a robust strategy for high-throughput in vivo evolution of c-di-AMP synthases.

INTRODUCTION

Cyclic diadenosine monophosphate (c-di-AMP), synthesized from two adenosine 5′-triphosphate (ATP) molecules by c-di-AMP synthases, functions as a second messenger regulating bacterial growth and homeostasis (Fig. 1A) (*1*–*4*). In addition, c-di-AMP can induce a conformational change in the stimulator of interferon genes (STING), activating downstream signaling cascades, including type I interferons and nuclear factor κB in mammalian cells (*5*–*9*). These pathways are crucial for initiating robust innate and adaptive immune responses against bacterial infections, making the activation of STING via c-di-AMP a promising strategy for immunotherapy (*10*, *11*). Given the low cellular permeability and instability of externally administered c-di-AMP, in situ production of this natural agonist by c-di-AMP synthases holds substantial potential in clinical therapy, ensuring ample intracellular levels to effectively activate STING (*12*, *13*). As a result, evaluating the in vivo activity of c-di-AMP synthases and engineering optimal candidates for therapy has gained great interest. However, progress is hindered by the lack of sensitive biosensors for high-throughput monitoring of c-di-AMP synthase activity in vivo.

The expanding availability of aptamers has greatly propelled the development of innovative biosensors (*14*). Aptamers are recognized for their high affinity toward specific targets and their unique ability to adopt intricate structures upon target binding, making them ideal for biosensor design. Riboswitch RNAs, a class of naturally occurring aptamers linked to expression platforms, undergo conformational changes upon binding specific metabolites or ions (*15*, *16*). This property enables riboswitches to regulate gene expression, transitioning between "OFF" and "ON" states upon binding their target molecules. This inherent responsiveness makes riboswitches prime candidates for biosensor applications. Researchers have harnessed the natural ligand-binding properties of riboswitches, modifying them to create biosensors capable of detecting various analytes (*17*, *18*). Furthermore, engineered riboswitches can be coupled with reporter genes, transducing binding events into readily measurable signals such as fluorescence or color changes. The versatility and programmability of riboswitches offer a robust and adaptable platform for identifying and quantifying biological and chemical substances. This enables riboswitches to be applied across diverse fields, including medical diagnostics, environmental monitoring, food safety, and synthetic biology.

C-di-AMP riboswitches are located in the 5′ untranslated region of mRNA and undergo conformational changes upon binding c-di-AMP, modulating the expression of genes involved in cell wall metabolism, ion transport, and osmotic stress response (*19*). Crystal structures of ligand-bound states reveal that a pseudo-symmetric riboswitch binds to two c-di-AMP molecules (Fig. 1, B and C), with dissociation constants (K_d) ranging from approximately 1 nM to 2.1 μM (*20*–*22*). This distinguishes it from most riboswitches, which typically exhibit a 1:1 ligand stoichiometry. The high specificity and sensitivity of c-di-AMP riboswitches make them promising candidates for developing biosensors to monitor intracellular c-di-AMP levels. However, the current structural knowledge is limited to the ligand-bound riboswitch, lacking structures for the ligand-free state. The absence of structural information regarding c-di-AMP–induced conformational changes in the riboswitch, coupled with its complex ligand-binding behavior, poses substantial challenges for developing a c-di-AMP biosensor based on the riboswitch. Furthermore, initial investigations into the *Bacillus subtilis* c-di-AMP riboswitch suggest that the RNA assumes a transcriptional OFF state upon c-di-AMP binding (*19*). Traditional OFF biosensors rely on a decrease in signal upon analyte binding, which can be limited by low signal-to-noise ratios. In contrast, ON biosensors offer distinct advantages by generating increasing signal upon analyte binding. This results in lower background noise, more easily identifiable output, higher signal-to-noise ratios, and ultimately, lower detection limits (*18*). Consequently, for high-throughput applications, ON biosensors are notably more advantageous than OFF biosensors. To leverage this benefit, the natural OFF function of the c-di-AMP riboswitch must be adapted to operate as an ON biosensor.

In this study, we sought to explore the dynamic landscape of a c-di-AMP riboswitch upon ligand binding to inform the rational design of a sensitive biosensor. To probe the riboswitch dynamics, we incorporated 11 Cy3-Cy5 fluorophore pairs into specific positions

---

[1]State Key Laboratory of Microbial Metabolism, School of Life Sciences and Biotechnology, Shanghai Jiao Tong University, Shanghai 200240, China. [2]School of Physics and Astronomy, Shanghai Jiao Tong University, Shanghai 200240, China.
*Corresponding author. Email: liuyu_sjtu@sjtu.edu.cn

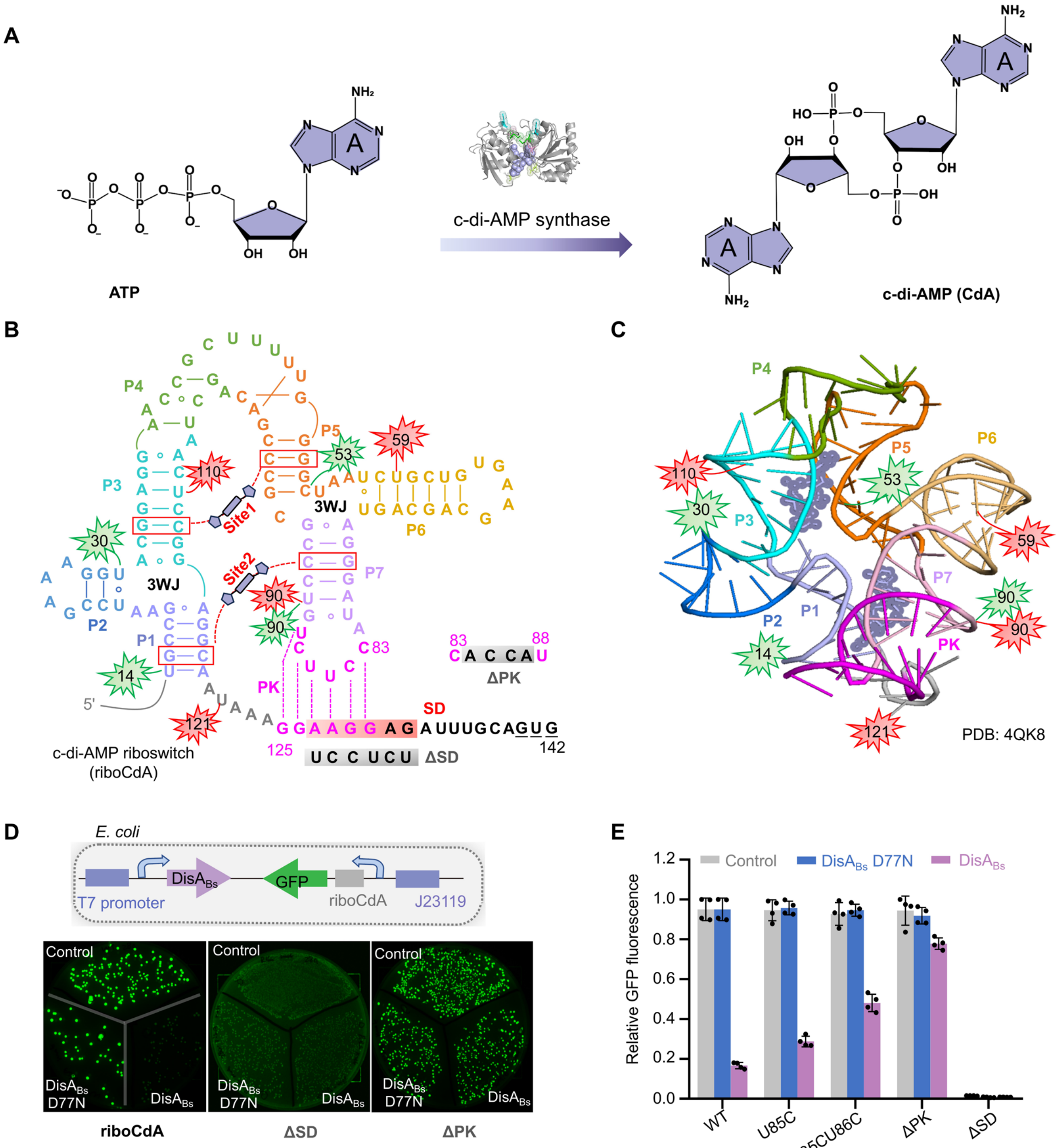

Fig. 1. Structure and function of c-di-AMP riboswitch. (**A**) C-di-AMP synthase catalyzes the conversion of two ATP molecules into one molecule of c-di-AMP (CdA). (**B**) Secondary structure of the translational c-di-AMP riboswitch (riboCdA) from *T. pseudethanolicus*. Binding of two molecules of c-di-AMP to a riboCdA mediates long-range PK (in magenta) formation, sequestering the proposed Shine-Dalgarno (SD) sequence (highlighted in red) and thereby repressing expression of downstream genes. The helices P1, P2, P3, P4, P5, P6, and P7 are depicted in light blue, blue, cyan, green, orange, gold, and light purple, respectively. The red and green sparkles represent the fluorophores Cy3 and Cy5, which were introduced into the RNA for smFRET studies. (**C**) Crystal structure of c-di-AMP riboswitch. Five Cy3-Cy5 pairs were incorporated into specific positions of riboCdA. (**D**) In vivo translation of riboCdA-controlled GFP gene. Two genetically encoded elements include GFP (in green) and T7 promoter-controlled c-di-AMP synthase DisA_{Bs} (in purple). The c-di-AMP molecules synthesized by DisA_{Bs} impair ribosome binding to riboCdA, thereby reducing GFP production. GFP production was affected by the PK mutations, and no significant production of GFP was observed in the presence of ΔSD-riboCdA. The mutations introduced in ΔSD- and ΔPK-riboCdA are highlighted in gray at (B). (**E**) Regulation of GFP expression by the WT (riboCdA), U85C, U85CU86C, ΔPK, and ΔSD mutation in the presence of DisA_{Bs} (purple) and DisA_{Bs} D77N (blue) in *E. coli*. GFP expression decreased in the presence of active c-di-AMP synthase, DisA_{Bs}, compared to the deactivated synthase, DisA_{Bs} D77N. WT, wild type; PDB, Protein Data Bank; 3WJ, three-way junction.

within the riboswitch and its mutants for single-molecule Förster resonance energy transfer (smFRET) assays. Our results reveal that the pseudoknot (PK) in the c-di-AMP riboswitch plays a regulatory role in gene expression and exhibits heightened sensitivity to both Mg^{2+} and c-di-AMP compared to other structurally important regions, such as helix P1, two binding sites, and three-way junctions (3WJs). Notably, the two c-di-AMP binding sites demonstrate cooperativity in modulating PK, with the distant site 1 exerting a more dominant effect. Our results highlight helix P1 as a crucial regulator of c-di-AMP sensitivity, as evidenced by smFRET, mutation, and in vivo gene expression experiments. A mutation in P1 can disrupt binding site 2, subtly shifting the specific binding and response spectrum of the riboswitch to c-di-AMP and expanding the detection limits for c-di-AMP by approximately 50-fold. To convert the c-di-AMP riboswitch output from a genetic OFF to ON state upon c-di-AMP binding, we rationally engineered its expression platform by incorporating an artificial stem loop to leverage a strand displacement strategy. Furthermore, the refined riboswitch-based biosensor exhibits potential for real-time detection of c-di-AMP and in vivo evolution of c-di-AMP synthases. It successfully identified a mutant c-di-AMP synthase exhibiting a sixfold improvement in activity and about 85% higher conversion efficiency from ATP to c-di-AMP within 10 min. Our findings demonstrate an approach for characterizing c-di-AMP synthases and provide a powerful tool for further investigation of this critical enzyme in cancer immunotherapy.

RESULTS

The PK plays a pivotal role in translational repression

The c-di-AMP riboswitch (riboCdA) studied here originates from *Thermoanaerobacter pseudethanolicus* and adopts a unique pseudo-symmetric structure characterized by two 3WJs connecting six helices (P1 to P3 and P5 to P7; Fig. 1, B and C) (*20*). Both c-di-AMP molecules interact with the riboswitch in a pseudo-twofold symmetric manner: one occupies site 1 between helices P3 and P5, while the other resides in binding site 2, flanked by helices P1 and P7 and capped by the PK (Fig. 1, B and C). The long-range PK (magenta) forms via base pairing between nucleotides 83 to 88 and 125 to 130 in the 3′ terminus. In contrast to the transcriptional termination mechanism observed in the *B. subtilis* c-di-AMP riboswitch (*19*, *21*), our riboCdA likely regulates gene expression at the translational level. This is inferred from the presence of a translation initiation codon (GUG, underlined in Fig. 1B) and potential pairing between the Shine-Dalgarno site (SD, highlighted in red in Fig. 1B) and 16*S* ribosomal RNA (fig. S1A). We propose that PK formation impedes ribosome binding to the SD, establishing the c-di-AMP–bound state as a translation OFF switch. This hypothesis found support in our in vivo experiments, wherein a green fluorescent protein–based gene reporter assay under the control of riboCdA detected an ~6-fold decreased signal upon T7 RNA polymerase-mediated expression of $DisA_{Bs}$ compared to expression of the inactivated mutant $DisA_{Bs}$-D77N (Fig. 1, D and E) (*23*, *24*). In addition, GFP repression by riboCdA was disrupted upon mutation of the SD or PK (Fig. 1, D and E). Moreover, a homologous riboCdA from *T. tengcongensis* MB4 also exhibited significant translation repression in response to c-di-AMP (fig. S1B). These findings suggest that the PK sequesters the SD sequence, preventing ribosome binding and thus inhibiting the translation of downstream genes.

The PK demonstrates sensitivity to both Mg^{2+} and c-di-AMP

The conformational changes of riboCdA remain obscure due to the lack of c-di-AMP–free structural information. To explore riboCdA dynamics at the single-molecule level using smFRET, we synthesized five distinct riboCdA samples, each labeled with Cy3 and Cy5 fluorophores at specific positions using position-selective labeling of RNA (PLOR), to monitor the dynamics of PK, binding sites 1 and 2, helix P1, and the overall folding of riboCdA (Fig. 2, A and B; fig. S2; and tables S1 to S5). Specifically, we used 17-step, 16-step, 13-step, 16-step, and 9-step PLOR reactions to synthesize Cy3/Cy5-labeled PK-, Site1-, Site2-, P1-, and 3WJ-riboCdA, respectively. PLOR uses a pause-restart transcription strategy in a solid-liquid hybrid state, pausing RNA synthesis at specific positions by missing certain types of nucleotide triphosphates (NTPs) and restarting RNA synthesis by adding a new NTP mix. This precise control over RNA synthesis allows for the precise labeling of Cy3 and Cy5 at the designated sites in the five-labeled samples (*25*, *26*). To investigate the impact of Cy3 and Cy5 placements on c-di-AMP binding in riboCdA, we conducted steady-state fluorescence titrations using samples labeled with 2-aminopurine (AP), Cy3 and Cy5, including AP/Cy3/Cy5-PK-riboCdA, AP/Cy3/Cy5-Site1-riboCdA, AP/Cy3/Cy5-Site2-riboCdA, AP/Cy3/Cy5-P1-riboCdA, and AP/Cy3/Cy5-3WJ-riboCdA, as well as their counterpart without Cy3/Cy5, 131AP-riboCdA, which was solely labeled with AP. These titrations yielded comparable half maximal effective concentration (EC_{50}) (fig. S3). The five modified AP/Cy3/Cy5-labeled riboCdA samples and the 131AP-riboCdA incorporate AP, a fluorescent adenosine analog, at site 131, replacing the native adenosine (A). This replacement enables fluorescent monitoring of riboCdA conformational changes with minimal structural perturbation. All AP/Cy3/Cy5-labeled riboCdA samples were synthesized using PLOR and PORVDA (position-specific labeling of RNA by DNAP variant). PORDVA is a recently developed method that enables the introduction of modifications at specific positions within RNA using an engineered DNA polymerase (*27*). This method has a distinct advantage in incorporating modifications at the 3′-end of long RNA. The detailed procedures and reagent usage for synthesizing the five AP/Cy3/Cy5-labeled riboCdA samples and the 131AP-riboCdA are listed in tables S1 to S6.

PK-riboCdA, labeled with Cy3 at site 90 and Cy5 at site 121, was synthesized to investigate PK folding under varying Mg^{2+} and c-di-AMP conditions (Fig. 2C, fig. S4 to S6, and table S1). In the absence of Mg^{2+} and c-di-AMP, a low-FRET peak ($E_{FRET} \sim 0.15$) was observed (Fig. 2D, gray). The addition of 1 mM Mg^{2+} induced a high-FRET state ($E_{FRET} \sim 0.75$, Fig. 2D, blue). Subsequent addition of 100 μM c-di-AMP further increased the proportion of the high-FRET state while notably reducing transitions between the low- and high-FRET states [Fig. 2, D (red) and E]. On the basis of the crystal structure of c-di-AMP–bound riboCdA, the distance between sites 90 and 121 is approximately 32 Å, corresponding to a FRET value of 0.7 to 0.8 (fig. S7). Thus, riboCdA adopts a PK-formed conformation in the presence of Mg^{2+}, and additional c-di-AMP (abbreviated as CdA) enhances both the proportion and stability of this conformation. Specifically, the addition of 100 μM c-di-AMP reduces the half-saturation point (EC_{50}) of Mg^{2+} for PK formation from approximately 0.91 to 0.42 mM (fig. S5A). When Mg^{2+} is below 2 mM, c-di-AMP presence leads to a more stable riboCdA, as evidenced by the lower measured k_{undock} values (fig. S5B).

Compared to the wild type (WT), ΔPK-riboCdA, which contains mutations disrupting the PK as shown in Fig. 1B, exhibited a significant decrease in the intensity of the high-FRET peak (Fig. 2F and table S7). Upon the addition of 1 mM Mg^{2+}, a dynamic mid-FRET state ($E_{FRET} \sim 0.53$) was observed, as evidenced by the transitions between the mid-FRET state and both the low-FRET state

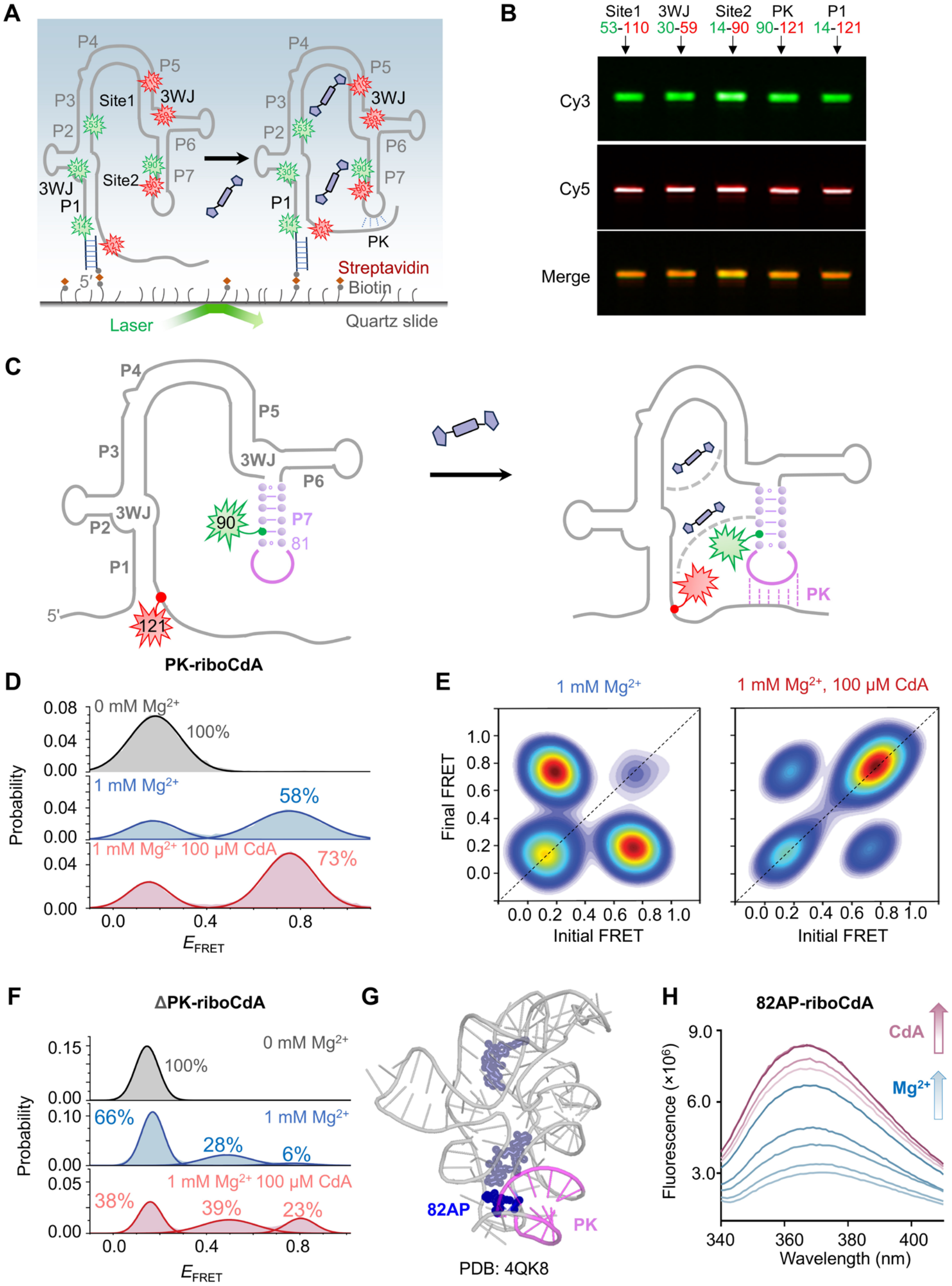

Fig. 2. Crucial roles of Mg^{2+} and c-di-AMP in PK formation and dynamics. (**A**) Schematic of smFRET experiments for riboCdA. The fluorophore-labeled riboCdA was immobilized on the slides via hybridization to a biotin-labeled oligonucleotide (gray line), with biotin depicted as a gray ball. (**B**) PAGE images of fluorophore-labeled RNA samples excited at 530-nm (top) and 650-nm (middle) fluorescent wavelengths. The bottom panel shows the merged images from the top and middle panels. (**C**) Schematic of PK-riboCdA. Cy3 and Cy5 were specifically labeled at sites 90 and 121, respectively. (**D**) Histograms for PK-riboCdA at 0 mM Mg^{2+} (gray), 1 mM Mg^{2+} (blue), and 1 mM Mg^{2+} with 100 μM c-di-AMP (red). (**E**) Transition occupancy density plots (TODPs) for PK-riboCdA at 1 mM Mg^{2+} and 1 mM Mg^{2+} with 100 μM c-di-AMP. (**F**) Histograms for ΔPK-riboCdA at 0 mM Mg^{2+} (gray), 1 mM Mg^{2+} (blue) and 1 mM Mg^{2+} with 100 μM c-di-AMP (red). (**G**) Structure of c-di-AMP–bound riboCdA with 82 (in blue) flipping out of L7. (**H**) Steady-state fluorescence spectra of 82AP-riboCdA titrated with 0 to 1 mM Mg^{2+} (blue) and 0 to 0.2 mM c-di-AMP in the presence of 1 mM Mg^{2+} (red). More than 300 single-molecule FRET trajectories were used to generate histograms in (D) and (F).

(E_{FRET} ~ 0.22) and the high-FRET state (E_{FRET} ~ 0.75) in transition occupation density plots and single-molecule traces (fig. S8). On the basis of the FRET value, we propose that in the mid-FRET state, the distance between sites 90 and 121 is closer than in the absence of Mg^{2+}, although the PK has not yet formed (fig. S8). In the presence of 1 mM Mg^{2+} and 100 μM CdA, the proportion of the high-FRET peak in ΔPK-riboCdA increased to approximately 23% (Fig. 2F, red), aligning with the repression percentage of GFP expression repression (~20%) induced by ΔPK-riboCdA (Fig. 1, D and E). These findings further support that the high-FRET peak represents the PK-formed conformation, which serves as a repressor in gene expression. In addition, the formation of the PK in response to Mg^{2+} and c-di-AMP was supported by steady-state fluorescence measurements of 82AP-riboCdA (Fig. 2, G and H; fig. S9; and table S8). In this construct, a fluorescent adenosine analog, AP, replaced an adenosine (A) at site 82 in the PK. This substitution preserves the base pairing within the PK while enabling the fluorescent tracking of PK changes. Upon the addition of either Mg^{2+} or c-di-AMP, a notable increase in fluorescence was observed in 82AP-riboCdA (Fig. 2, G and H), aligning with the site 82 flipping out of L7 as observed in the crystal structure of c-di-AMP–bound riboCdA (Fig. 2G). These results validate that the dynamics of the PK in riboCdA respond sensitively to both Mg^{2+} and c-di-AMP, consistent with our smFRET observations.

Key structural regions of riboCdA exhibit distinct responses to c-di-AMP

In addition to the PK, we studied the impact of c-di-AMP on other key regions of riboCdA, including helix P1, binding site 1, site 2, and 3WJs. Helix P1, as a component of binding site 2 and located near the PK, is anticipated to play a notable role in both c-di-AMP binding and PK dynamics. Cy3 and Cy5 fluorophores were placed at sites 14 and 121 of riboCdA to create P1-riboCdA for probing the dynamics of helix P1 via smFRET (Fig. 3A, fig. S10, and table S4). At 0 to 5 mM Mg^{2+}, a high-FRET peak (E_{FRET} ~ 0.8) was evident in the smFRET histograms of P1-riboCdA (Fig. 3A and fig. S11). The E_{FRET} value of 0.8 correlates well with the distance between sites 14 and 121 in the c-di-AMP–bound riboCdA structure (fig. S7), indicating that Mg^{2+} is sufficient to stabilize P1. The addition of 100 μM c-di-AMP caused a broader distribution of the peak, suggesting increased flexibility of helix P1 (Fig. 3A). To investigate the dynamics of binding site 1 in riboCdA, we synthesized site1-riboCdA labeled with Cy3 and Cy5 at sites 53 and 110, respectively, for smFRET assays (Fig. 3B, fig. S12, and table S2). In the absence of Mg^{2+}, a low-FRET state (E_{FRET} ~ 0.35) indicated that helices P3 and P5 are spatially distant and unable to form binding site 1 (fig. S13B). Upon the addition of Mg^{2+}, E_{FRET} increased from approximately 0.35 at 0 mM Mg^{2+} to 0.52 at 5 mM Mg^{2+}, indicating closer proximity between helices P3 and P5 (fig. S13B). The subsequent addition of 5 to 100 μM c-di-AMP induced a stable high-FRET state (E_{FRET} ~ 0.77), corresponding to the folded state of binding site 1 in the crystal structure (Fig. 3B and figs. S7 and 13). In addition, the proportions of the high-FRET peak correlate positively with c-di-AMP concentrations. To assess c-di-AMP influence on binding site 1, we synthesized 103AP-riboCdA, where AP is introduced at site 103 situated in the linker between helices P3 and P5 (fig. S14, A to C, and table S9). Minimal fluorescence change was detected in 103AP-riboCdA upon the addition of 1 mM Mg^{2+} (fig. S14D). Conversely, upon the addition of c-di-AMP, a significant increase in fluorescence was observed in 103AP-riboCdA (fig. S14D). These results support the conclusions drawn from the smFRET assays of site1-riboCdA: c-di-AMP is essential for the formation of binding site 1, whereas Mg^{2+} alone is unable to construct the binding site 1 despite its role in bringing P3 and P5 closer together to facilitate c-di-AMP binding.

Subsequently, we synthesized site2-riboCdA with Cy3 and Cy5 labeled at sites 14 and 90, respectively (Fig. 3C, fig. S15, and table S3). Unlike binding site 1, Mg^{2+} alone can adjust the helices P1 and P7, forming two dynamic structures with E_{FRET} of approximately 0.43 and 0.2, respectively (Fig. 3C and fig. S16). Unexpectedly, in the presence of Mg^{2+}, adding 100 μM c-di-AMP to site2-riboCdA shifted the E_{FRET} ~ 0.43 peak to a lower FRET peak (~0.35) (Fig. 3C and fig. S16). This indicates that c-di-AMP induced local conformation rearrangements to accommodate the ligand at the binding site 2. In contrast to the functional regions, the overall folding of riboCdA between two 3WJs became only marginally compact upon the addition of c-di-AMP. This is reflected in E_{FRET} values of 3WJ-riboCdA, which increased from approximately 0.36 to 0.38 upon the addition of 100 μM c-di-AMP (Fig. 3D, fig. S17, and table S5). Collectively, the PK, two binding sites, and helix P1 displayed distinct responses to c-di-AMP. Kinetic analysis revealed that the PK exhibited higher dynamics at low c-di-AMP, indicated by its higher k_{undock} compared to the binding site–labeled design (Fig. 3E). In response to Mg^{2+} and c-di-AMP, the PK demonstrated greater sensitivity than the binding sites and helix P1 (Fig. 3, F and G). A surprising finding was that, despite the structural similarities observed in the crystal structure, the two binding sites exhibited significant differences in their kinetics behavior upon receiving the c-di-AMP signal, as shown by the k_{dock} and k_{undock} values in Fig. 3E. Consequently, we propose a model that incorporates the kinetic information for riboCdA folding upon c-di-AMP binding (fig. S18).

Modifying P1 heightens the PK's sensitivity to c-di-AMP

To broaden the c-di-AMP response range of riboCdA, we generated a series of mutants, including Δsite1-riboCdA, Δsite2-riboCdA, 2bP1-riboCdA, and ΔP1-riboCdA to disrupt binding site 1, site 2, and helix P1, respectively (Fig. 4A, figs. S19 and 20, and tables S10 to S13). The Cy3-Cy5 pair was incorporated into sites 90 and 121 in all four mutants to monitor PK dynamics using smFRET (Fig. 4, B to E). In Δsite1-PK-riboCdA and Δsite2-PK-riboCdA, the high-FRET peak increased with c-di-AMP up to 100 μM in the presence of 0.75 mM Mg^{2+} (Fig. 4F). Disrupting binding site 1 impaired PK formation of riboCdA more significantly compared to binding site 2 (EC_{50}: ~78.9 μM versus 11.0 μM). In contrast, the high-FRET state in 2bP1-PK-riboCdA exhibited response to 0.05 to 500 μM c-di-AMP, a much broader range compared to WT and other mutants (Fig. 4G). As expected, 2bP1-riboCdA showed an inhibitory effect on in vivo GFP translation, as the two residues mutated in 2bP1-riboCdA to reduce base pairs in P1 from four to two and also impairs binding site 2 (Fig. 4, A and H). However, compared to WT, the modified 2bP1-riboCdA triggered significantly higher PK dynamics (Fig. 4I). In addition, disrupting binding site 1 (Δsite1) resulted in a greater impairment of PK formation and in vivo function of riboCdA compared to disrupting binding site 2 (Δsite2) (Fig. 4H). This aligns with the lower proportion of high-FRET peak in Δsite1-PK-riboCdA compared to Δsite2-PK-riboCdA (Fig. 4, B and C). Notably, in the absence of c-di-AMP, disrupting site 1 led to fewer molecules adopting the high-FRET conformation compared to disrupting site 2, indicating that site 1 plays a more substantial role in PK formation in

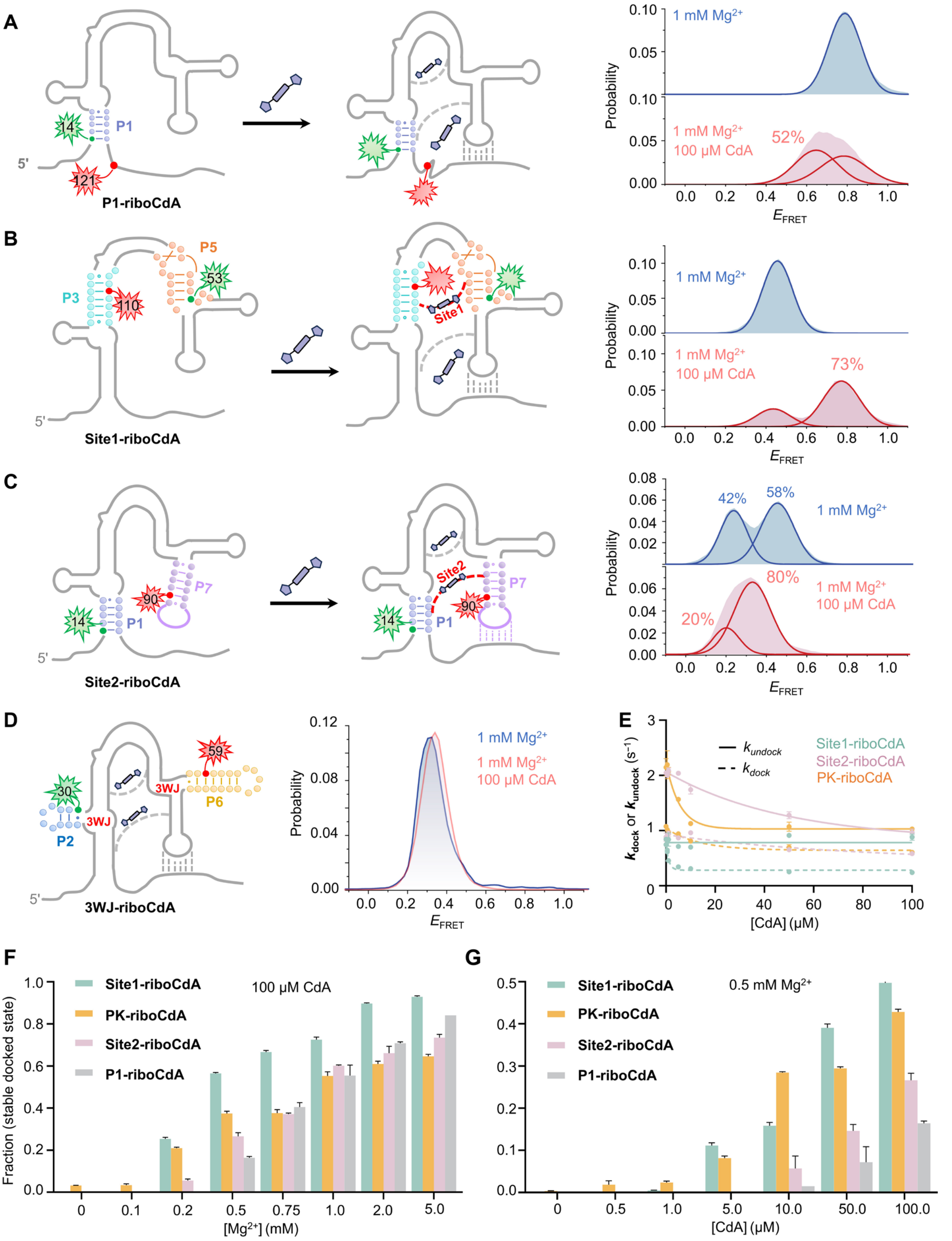

Fig. 3. smFRET measurements of P1-, Site1-, Site2-, and 3WJ-riboCdA. (**A** to **D**) FRET histograms of P1-riboCdA (A), Site1-riboCdA (B), Site2-riboCdA (C), and 3WJ-riboCdA (D) at 1.0 mM Mg^{2+} in the absence (blue) and presence (red) of 100 μM c-di-AMP. The Cy3 and Cy5 are depicted as green and red sparkles, respectively. (**E**) Rate constants, k_{dock} and k_{undock}, between low- and high-FRET states of PK-riboCdA (orange), Site1-riboCdA (green), and Site2-riboCdA (purple) plotted with c-di-AMP concentrations. (**F**) Normalized proportions of stable high-FRET states in Site1-riboCdA (green), PK-riboCdA (orange), Site2-riboCdA (purple), and P1-riboCdA (gray) plotted with Mg^{2+} concentrations in the presence of 100 μM c-di-AMP. (**G**) Normalized proportions of stable high-FRET states in Site1-riboCdA (green), PK-riboCdA (orange), Site2-riboCdA (purple), and P1-riboCdA (gray) plotted with c-di-AMP concentrations in the presence of 0.5 mM Mg^{2+}.

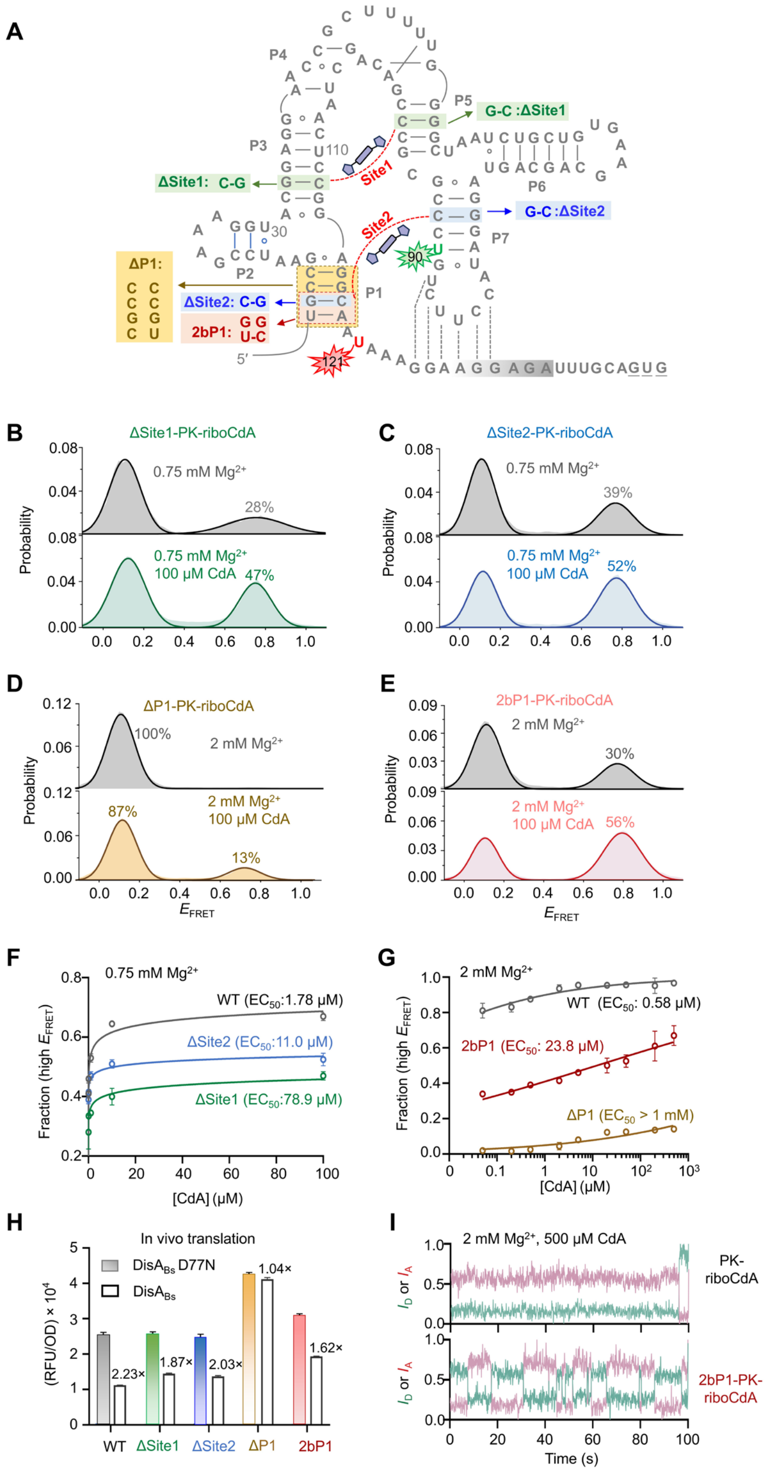

Fig. 4. Mutations in the binding sites or P1 impair PK formation and function. (**A**) Secondary structure of PK-riboCdA. Cy3 at site 90 and Cy5 at site 121 are depicted as green and red sparkles, respectively. The mutations in ΔSite1-, ΔSite2-, 2bP1-, and ΔP1-PK-riboCdA are highlighted in green, blue, red, and gold, respectively. (**B** to **E**) FRET histograms of ΔSite1-PK-riboCdA (B), ΔSite2-PK-riboCdA (C), ΔP1-PK-riboCdA (D), and 2bP1-PK-riboCdA (E) at 0.75 or 2 mM Mg^{2+} in the absence (gray) and presence of 100 μM c-di-AMP. (**F**) Normalized proportions of high-FRET states for PK-riboCdA (gray), ΔSite1-PK-riboCdA (green), and ΔSite2-PK-riboCdA (blue) plotted with c-di-AMP concentrations. (**G**) Normalized proportions of high-FRET states for PK-riboCdA (gray), 2bP1-PK-riboCdA (red), and ΔP1-PK-riboCdA (brown) plotted with c-di-AMP concentrations. (**H**) In vivo translation repression assay for the WT and the mutants of riboCdA. (**I**) Representative single-molecule traces of PK-riboCdA (top) and 2bP1-PK-riboCdA at 2 mM Mg^{2+} and 500 μM c-di-AMP. Intensity of donor (I_D, Cy3) and acceptor (I_A, Cy5) are shown in green and purple lines. RFU, relative fluorescence unit; OD, optical density.

the absence of c-di-AMP. However, the addition of a high concentration of c-di-AMP stabilized the PK, thereby reducing the differences of the two binding sites (Fig. 4, B and C). These findings suggest that despite binding site 1 being farther from PK than site 2, it plays a pivotal role in PK. The distal yet dominant role of site 1 is sufficient to induce dynamic PK regulation of translation, even with a truncated P1 and disrupted site 2 in 2bP1-riboCdA (fig. S18). Eliminating the synergistic effect between binding sites 1 and 2 while retaining only site 1 broadens the c-di-AMP detection spectrum of riboCdA.

Inverting the switch characteristics of riboCdA

The natural c-di-AMP riboswitch produces an OFF signal upon receiving c-di-AMP, which is not ideal for rapid screening. To conceptually transform riboCdA into a desirable ON biosensor, we introduced a 10-nt oligonucleotide probe complementary to the riboCdA terminus to release the SD from PK (Fig. 5A). In the absence of c-di-AMP, hybridization between the probe and the SD prevented PK formation, as evidenced by the predominant low-FRET peak observed in the smFRET analysis (Fig. 5B). However, the presence of c-di-AMP substantially promoted PK formation via strand displacement, leading to increased dissociation of the free probe and a shift of the dominant peak from low-FRET to high-FRET (Fig. 5B and fig. S21). Using a Cy5-labeled 10-nt probe, WT, 2bP1-riboCdA, and ΔP1-riboCdA exhibit notable differences in probe dissociation at 2 mM Mg^{2+} and 37°C, with measured EC_{50} of 1.8, 191, and 6396 μM, respectively (Fig. 5, C to E). In addition, the apparent cooperativity coefficients decreased to 0.8 for 2bP1-riboCdA, decreased to 0.5 for ΔP1-riboCdA, and remained at 1.8 for WT, which is consistent with the disruption of at least one binding site in the mutated riboCdA.

To adapt riboCdA into a biosensor capable of binding c-di-AMP and generating an ON signal, we designed an artificial stem loop. This stem loop, positioned between helix P1 and 3′-end, incorporated a complementary probe and the SD region within its structure (Fig. 5F). Crucially, the riboswitch expression platform was reengineered so that the SD sequence forms a stable stem loop in the absence of ligand, with which PK formation competes upon ligand binding. The addition of c-di-AMP is expected to favor PK formation, thereby competing with the engineered stem loop via strand displacement. This simultaneously releases the single-stranded SD, permitting ribosome binding and translation initiation. To engineer riboCdA for enhanced sensitivity to c-di-AMP, we randomized both the base pairing (9 to 12 combinations of G-C, A-U Watson-Crick pairs, and G-U wobble pairs) and loop sizes (4 to 11 nt) within the stem-loop structure (fig. S22). Among the eight tested variants, D4, which has an 11–base paired stem and a 7-nt loop, was proved to be the most effective. In the presence of c-di-AMP synthase $DisA_{Bs}$, the GFP production of ON-riboCdA increased by 7.6-fold compared to its deactivated counterpart, D77N (Fig. 5, G and H). Agar plate images further supported the successful inversion of our engineered biosensor from OFF to ON (Fig. 5I). In the presence of deactivated synthase D77N, the formation of stem-loop D4 in ON-riboCdA rendered the SD inaccessible to ribosomes, effectively switching GFP translation OFF. In contrast, in the presence of $DisA_{Bs}$, the in vivo produced c-di-AMP disrupted the stability of D4, triggering strand displacement to promote PK formation. This process liberated the SD and the initiation codon, enabling ribosome binding and GFP translation (Fig. 5I, right).

The introduction of the stem-loop D4 enables ON-riboCdA to achieve the desired ON switch behavior. To further characterize the activities of c-di-AMP synthases on a larger scale, we engineered 2bP1-riboCdA by incorporating D4, generating ON-2bP1-riboCdA. This construct, along with ON-riboCdA and ON-ΔP1-riboCdA, was used to assess the enzymatic activities of six bacterial c-di-AMP synthases (fig. S23). As illustrated in Fig. 5J, $CdaA_{Lm}$, $CdaA_{Bs}$, and $DisA_{Bs}$ displayed heightened sensitivity in both ON-2bP1-riboCdA and ON-riboCdA compared to other c-di-AMP synthases. This observation aligns with our findings in riboCdA despite a decrease in translation efficiency with these effective c-di-AMP synthases. These results validate that our engineered ON-riboCdA and ON-2bP1-riboCdA can effectively discriminate between different c-di-AMP synthases in living cells using ON signals, highlighting their adaptability as c-di-AMP biosensors.

Advancement in c-di-AMP synthase engineering

C-di-AMP synthases, prevalent in various gram-positive bacteria, catalyze c-di-AMP synthesis and hold promise for therapeutic applications, particularly in tumor treatment (*12*, *13*, *28*). Nevertheless, the lack of biosensors for evaluating the in vivo functionality of c-di-AMP synthases hinders the on-site screening of mutated enzymes to identify superior variants. We devised a strategy to screen $DisA_{Bs}$ mutants using ON-2bP1-riboCdA or ON-riboCdA as in vivo biosensors, aiming to enhance the enzyme's ability for local c-di-AMP production (Fig. 6A). To demonstrate the efficacy of our engineered ON biosensor, we selected WT $DisA_{Bs}$ as the parent enzyme for enhancement. We conducted site-saturation mutagenesis on nine residues (E53, D56, M97, A100, M109, T113, E130, R131, and R132; fig. S24) located within the catalytic pocket while not directly involved in c-di-AMP synthesis using a degenerate NNK codon. Plasmids carrying mutated $DisA_{Bs}$, along with either ON-2bP1-riboCdA or ON-riboCdA and a GFP reporter gene, were transformed into the *Escherichia coli* strain BL21(DE3) and plated onto the LB agar. Clones exhibiting the highest green fluorescence on the plates were selected for sequencing (Fig. 6A). Both ON-riboCdA and ON-2bP1-riboCdA are well-suited for fluorescence-based screening. Using ON-riboCdA as a biosensor, we identified three highly responsive variants: E53P, E130K, and M97L (fig. S24). Using ON-2bP1-riboCdA, we identified three additional variants—E53A, E130R, and D56S—that displayed responsiveness to c-di-AMP (Fig. 6B). Among these mutants exhibiting enhanced activity, E130K demonstrated advantages in c-di-AMP production, leading to more efficient GFP expression within a shorter timeframe (Fig. 6, A to C). In addition, the lower in vivo enzymatic activities of E53A, E130R, and D56S compared to E53P, E130K, or M97L highlight the superiority of ON-2bP1-riboCdA in detecting c-di-AMP synthases, offering higher sensitivity and a broader detection spectrum (Fig. 6C).

To tentatively optimize mutant performance, we generated and tested combinations of the identified mutations with enhanced activities. Notably, E130K outperformed all tested combined mutants—including the double mutant P + K (E53P + E130K), the triple mutant P + K + L (E53P + E130K + M97L), and the quadruple mutant P + K + S + L (E53P + E130K + M97L + D56S)—in terms of in vitro c-di-AMP production, as demonstrated by high-performance liquid chromatography (HPLC) analysis (Fig. 6, D and E, and fig. S25). Specifically, the single E130K mutation yielded a remarkable 6.2-fold increase in c-di-AMP production compared to WT $DisA_{Bs}$. The E130K mutation significantly enhanced catalytic efficiency, improving the conversion from ATP to c-di-AMP from less than 10% to more than 95% within 30 min, as evidenced by our HPLC results

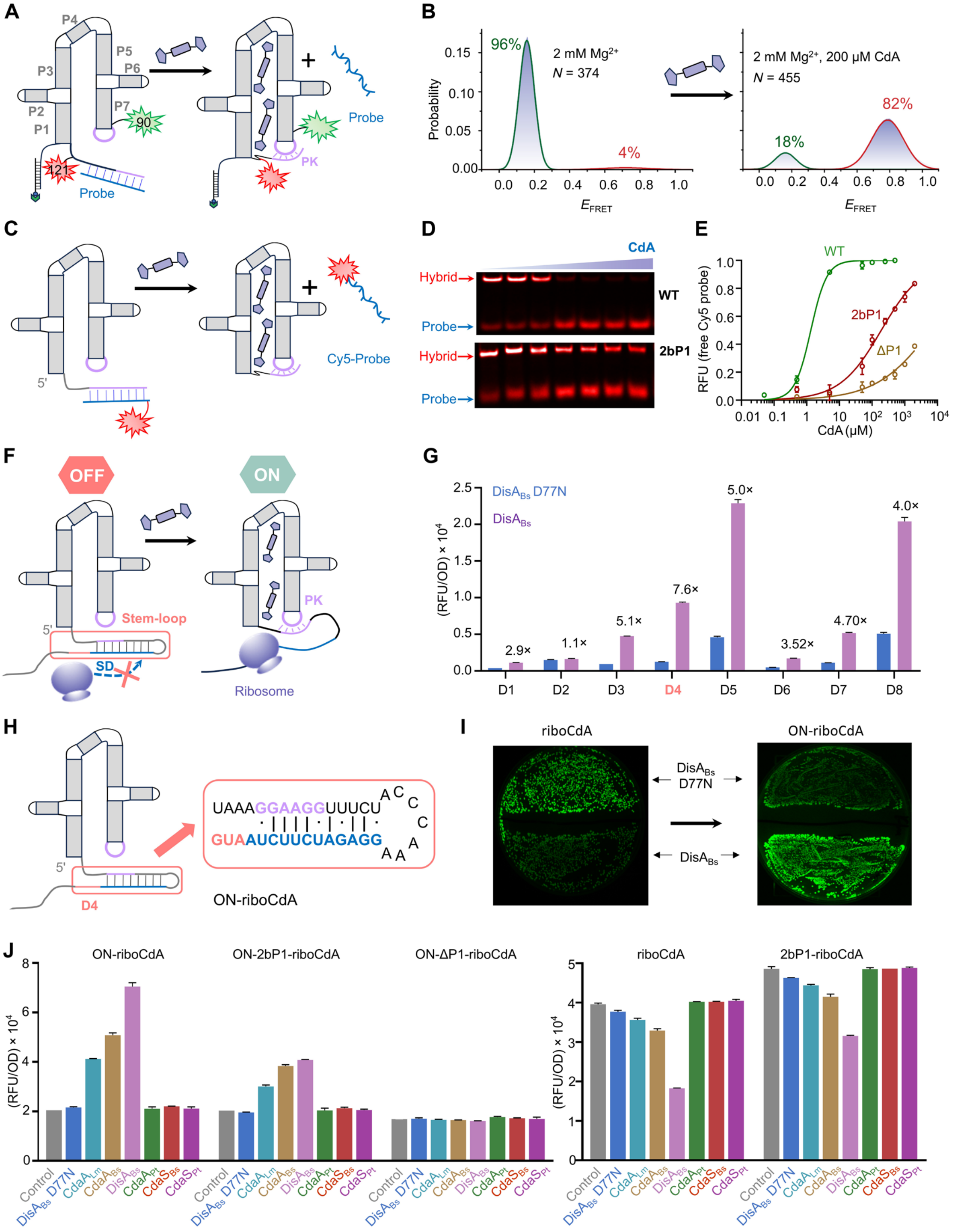

Fig. 5. Inverting riboCdA from OFF to ON biosensor. (**A**) Schematic of PK formation via strand displacement in the presence of a probe. The addition of c-di-AMP dissociates the DNA probe (blue line) from riboCdA, triggering PK formation. (**B**) smFRET histograms for PK-riboCdA in the presence of the probe at 2 mM Mg^{2+} with and without 200 μM c-di-AMP. (**C**) Schematic of c-di-AMP addition to dissociate the Cy5-labeled probe from riboCdA at 2 mM Mg^{2+} and 37°C. (**D**) Denaturing PAGE images showing dissociation of the Cy5-probe from riboCdA (WT, top) and 2bP1-riboCdA (bottom) upon the addition of c-di-AMP. The gels were excited using a 630 nm fluorescent wavelength. (**E**) Fitting of relative fluorescence unit (RFU) for riboCdA (green), 2bP1-riboCdA (red), and ΔP1-riboCdA (brown) plotted with c-di-AMP concentrations. (**F**) Schematic of inverting riboCdA from OFF to ON biosensor via strand displacement. c-di-AMP, synthesized from $DisA_{Bs}$, disrupts the stem-loop structure, releasing the SD sequence for ribosome binding. (**G**) In vivo translation activities of stem loops D1 to D8, with D4 exhibiting the highest up-regulation folds. (**H**) Predicted secondary structure of D4, with PK in purple, SD in blue, and the translation initiation codon in red. (**I**) Fluorescent images of agar plates from in vivo translation experiments, showing GFP production regulated by riboCdA (left) and ON-riboCdA (right). (**J**) Comparison of activity among $CdaA_{Lm}$ (cyan), $CdaA_{Bs}$ (brown), $DisA_{Bs}$ (light purple), $CdaA_{Pt}$ (green), $CdaS_{Bs}$ (red), and $CdaS_{Pt}$ (purple) using ON-riboCdA, ON-2bP1-riboCdA, ON-ΔP1-riboCdA, riboCdA, and 2bP1-riboCdA as biosensors.

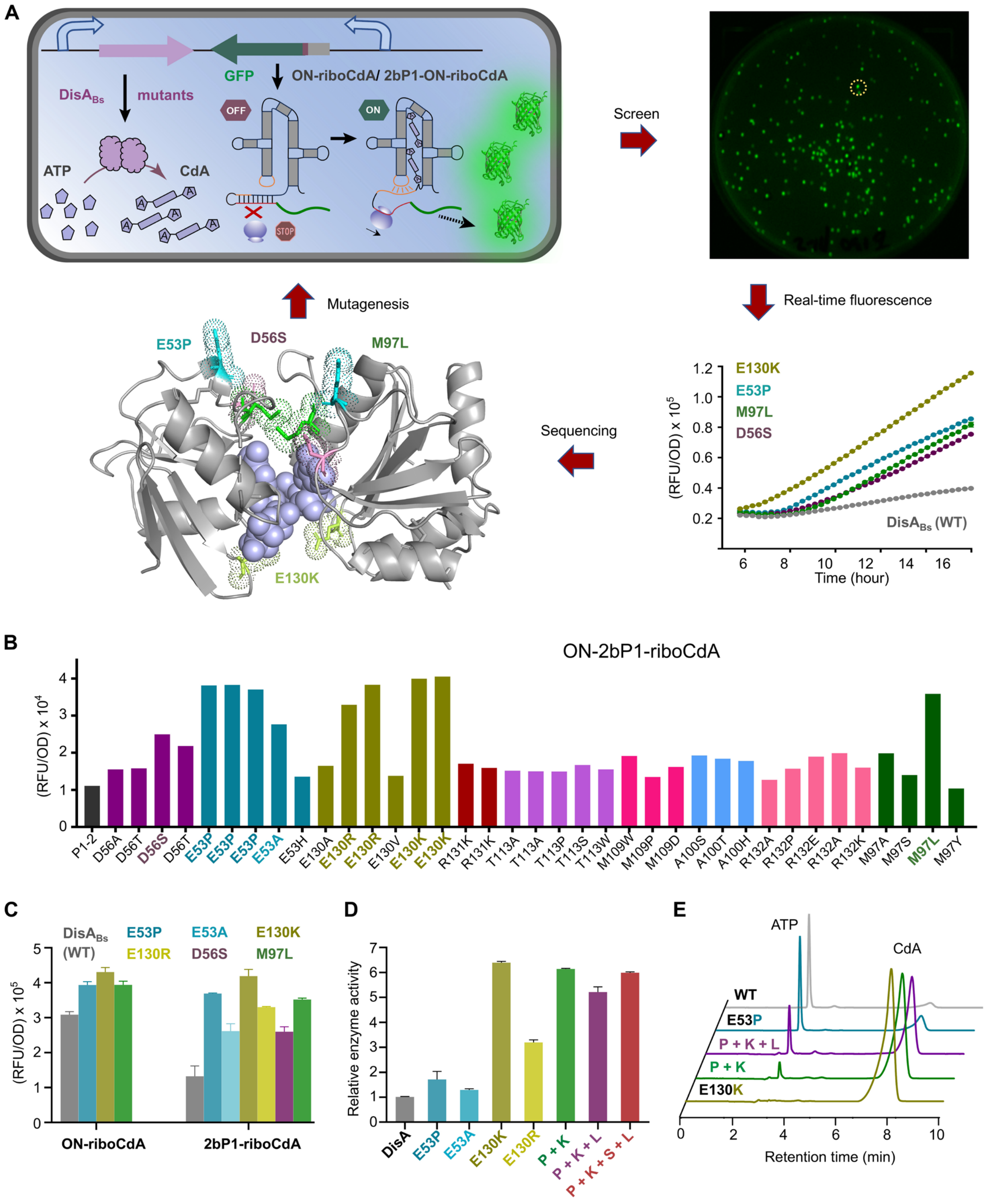

Fig. 6. Utilization of ON biosensor for engineering c-di-AMP synthases. (**A**) Schematic procedures for rapid screening using our designed ON-riboCdA or ON-2bP1-riboCdA biosensors. Site-saturated mutants of DisA$_{Bs}$ are screened on the basis of real-time measurements of GFP fluorescence in the presence of c-di-AMP in *E. coli* BL21 (DE3). The optimal-performance mutants screened using ON-riboCdA or ON-2bP1-riboCdA biosensors are then sequenced and characterized. (**B** and **C**) Three and six mutants exhibiting higher enzymatic activities compared to the WT (DisA$_{Bs}$) were identified using ON-riboCdA or ON-2bP1-riboCdA biosensors, respectively. (**D**) In vitro activity comparison among DisA$_{Bs}$, selected superior mutants, and combined mutants. (**E**) HPLC spectra showing the conversion of c-di-AMP from ATP at 30 min using DisA$_{Bs}$ (black), E53P (cyan), P+K+L (purple), P+K (green), and E130K (brown).

(Fig. 6E and fig. S25). This remarkable outcome is supported by the analysis of the crystal structure. In the c-di-AMP–bound $\mathrm{DisA_{Bs}}$ crystal structure, residue 130 is situated near the c-di-AMP binding site (fig. S24). Replacing the glutamic acid (E) with lysine (K) at residue 130 significantly increases the positively charged surface of the $\mathrm{DisA_{Bs}}$, potentially mitigating the electrostatic repulsion between the negatively charged c-di-AMP and $\mathrm{DisA_{Bs}}$, thereby enhancing their interaction (fig. S24C). Furthermore, as illustrated in fig. S26, seven $\mathrm{DisA_{Bs}}$ mutants exhibited higher activity compared to the well-characterized c-di-AMP synthase DacA in the therapeutic *E. coli* Nissle (EcN) 1917 (*13*, *29*–*31*).

DISCUSSION

The c-di-AMP plays a dual role as both a crucial secondary messenger within bacteria, regulating essential physiological processes, and a potent agonist of the STING pathway in host cells, eliciting innate immune responses against infections. On-site synthesis of c-di-AMP is preferable to exogenous delivery for several reasons. These include mitigating off-target effects, overcoming the challenges of low membrane permeability, and circumventing rapid degradation. Therefore, enhancing the catalytic efficiency of c-di-AMP synthases is paramount. However, engineering these enzymes has been hampered by the lack of efficient screening methods. C-di-AMP riboswitches, with their remarkable ability to specifically recognize and bind to c-di-AMP, offer a promising avenue for developing these tools. Inspired by this inherent capability of riboswitches, we sought to engineer a c-di-AMP–responsive riboswitch as a RNA biosensor for identifying highly efficient c-di-AMP synthases. However, this endeavor faces immediate challenges. First, our understanding of the dynamic structural changes that occur upon c-di-AMP binding remains limited. Second, naturally occurring c-di-AMP riboswitches exhibit an undesirable OFF signal upon binding to c-di-AMP.

To address the challenges, we investigated the dynamic mechanism and regulatory function of the full-length c-di-AMP riboswitch. Using a combination of single-molecule FRET, fluorescence titration, mutagenesis, and in vivo gene expression assays, we were able to probe the intricate interplay between structure and function. Our results highlight notable variations in the dynamics and c-di-AMP response across different structurally important regions of the riboswitch. Our findings revealed a pivotal role for the PK in sensing c-di-AMP, ultimately governing gene expression. The efficacy of PK is closely tied to the cooperative functionality of the two c-di-AMP binding sites, particularly site 1. The ligand-sensing mechanism of the c-di-AMP riboswitch shares similarities with that of T-box riboswitch (*32*, *33*). PK is a canonic long-range interaction shared by many riboswitches, such as preQ1 and SAM-II riboswitches, and the ligand-binding that favors the proximal PK has been widely discussed in literature (*34*–*36*). However, the c-di-AMP riboswitch harbors a unique structure, containing two distant binding sites, which is different from most riboswitches. Isothermal titration calorimetry (ITC) of a transcriptionally regulated c-di-AMP riboswitch from *B. Subtilis* revealed that the deletion of site 1 hampered site 2, whereas the deletion of site 2 had a weaker influence on site 1 (*20*). The unbalanced cooperativity between the two binding sites was also observed in our translationally regulated c-di-AMP riboswitch based on smFRET data. It has been reported that riboswitches obey kinetic control in modulating gene expression (*37*, *38*). In the case of riboCdA, site 1 (distal to the PK) adopts less dynamic conformations with a weak disassociation rate, whereas site 2 (proximal to the PK) folds into much more dynamic conformations in the presence of c-di-AMP. However, the folding of both site 1 and site 2 facilitates the formation of PK, as supported by our observations in smFRET and in vivo experiments, which show that the mutations in site 1 or site 2 impaired the formation and function of the PK in riboCdA. The dynamics-guided engineering of riboCdA to 2bP1-riboCdA weakens the synergistic effect between binding sites 1 and 2, broadening the c-di-AMP detection spectrum of the c-di-AMP riboswitch. This strategy can be applied to engineer other RNAs, especially those without determinated ligand-free structures, to adjust their binding capacity and biological functions based on their dynamic landscape.

Helix P1, a component of binding site 2 and situated near the functional core of the riboswitch (PK), emerged as a promising target for engineering PK functionality due to its crucial role in the cooperative binding of c-di-AMP. Introducing subtle mutations into helix P1 successfully disrupted this cooperative interaction while preserving dominant c-di-AMP binding at site 1. This loosened the riboswitch's grip on c-di-AMP, effectively broadening its detection range by approximately 50-fold. Furthermore, drawing upon our dynamic data and the strand displacement strategy, we rationally modified the P1-mutated riboswitch by introducing an artificial stem loop. This modification successfully inverted the riboswitch's output signal in response to c-di-AMP. Using this engineered riboswitch, we rapidly evolved a c-di-AMP synthase mutant, E130K, exhibiting an over sixfold enhancement in catalytic efficiency compared to its parent enzyme. Crucially, this single mutation markedly improved the conversion efficiency from ATP to c-di-AMP, escalating from less than 10% in the WT to more than 95% within a mere 10 min. Moreover, this mutation showed superior activity to the well-established c-di-AMP synthase DacA in the therapeutic EcN 1917 strain. The strand displacement strategy used in engineering riboCdA has been reported in natural riboswitches, such as fluoride and ZTP riboswitches (*39*, *40*). This approach is efficient in inverting the regulatory function of riboCdA and can potentially be applied to other RNA aptamers.

RNA molecules play critical regulatory roles within cells, driving the rapid advancement of RNA-based biotechnology (*41*–*43*). Engineering natural RNA molecules for biological functions and applications is urgently needed. Dynamic studies of RNA provide not only structural information but also crucial insights for engineering RNA to meet diverse needs in synthetic biology, therapeutics, environmental science, and biomanufacturing (*44*–*46*). In this study, we leveraged comprehensive dynamic findings of the c-di-AMP riboswitch and strand displacement strategy to design a c-di-AMP biosensor. This RNA biosensor is capable of accelerating the directed evolution of c-di-AMP syntheses, holding potential value for applications such as tumor therapy. Given the inherently dynamic nature of RNA, constructing RNA tools based on a deep understanding of their dynamic behavior will stimulate a wave of innovation, broadening the applications and impact of RNA technologies.

MATERIALS AND METHODS

Materials

The primers and oligonucleotides used for site-directed mutagenesis and smFRET were purchased from Sangon Biotech (Shanghai, China) and listed in tables S15 and S16. The c-di-AMP was purchased from MedChemExpress (New Jersey, USA). Modified nucleotides triphosphate were purchased from APExBIO Technology (Houston, USA). Other chemicals were purchased from Sigma-Aldrich (Saint Louis, USA) and Sangon (China).

Plasmid construction

The J23119-riboCdA-GFP gene was purchased from Sangon (China) and cloned into pET28a(+) to generate pET28a-riboCdA-GFP plasmid. An *E. coli* codon-optimized gene for DisA$_{Bs}$ expression was ordered from Sangon and inserted into pET28a-riboCdA-sfGFP between *NdeI* and *XhoI* sites, resulting in the plasmid of pET28a-DisA$_{Bs}$-riboCdA-GFP. Site-directed mutagenesis was conducted using inverse polymerase chain reaction (iPCR) to introduce mutations in riboCdA and in DisA$_{Bs}$. The mutated products were digested with Dpn I (TAKARA, Japan) at 37°C for 30 min, followed by ligation using the ClonExpress One Step Cloning Kit (Vazyme, China). The ligated products were then transformed into *E. coli* BL21 (DE3) competent cells, plated on LB agar medium supplemented with kanamycin (50 mg/liter), and measured using 480-nm fluorescent excitation on a ChemiScope 6200 gel imager (Clinx Company, China).

Synthesis of unlabeled RNA

The unlabeled RNA—including riboCdA, 130 nt-riboCdA, ΔP1-riboCdA, and 2bP1-riboCdA—were synthesized by in vitro transcription (IVT): 0.5 μM DNA template was incubated with 0.3 μM T7 RNAP in the buffer [200 mM Hepes, 28 mM $MgCl_2$, 6 mM NTP, and 20 mM dithiothreitol (DTT) (pH 8.0)] for 2 to 4 hours at 37°C. Subsequently, the RNA products were purified using 12% denaturing urea–polyacrylamide gel electrophoresis (PAGE). The RNA sequences are listed in tables S6 and S15.

Synthesis of fluorophore-labeled RNA

The labeled riboCdA samples—including PK-riboCdA, ΔPK-riboCdA, Δsite1-PK-riboCdA, Δsite2-PK-riboCdA, ΔP1-PK-riboCdA, 2bP1-PK-riboCdA, site1-riboCdA, site2-riboCdA, P1-riboCdA, 3WJ-riboCdA, 130nt-PK-riboCdA, 130nt-site1-riboCdA, 130nt-site2-riboCdA, 130nt-P1-riboCdA, 130nt-3WJ-riboCdA, 82AP-riboCdA and 103AP-riboCdA—were synthesized by PLOR as previously described (*25*, *26*). DNA and RNA sequences used in PLOR reactions are listed in tables S14 and S15. Detailed procedures and reagent additions for each labeled sample are provided in tables S1 to S5 and S7 to S13. Biotin-tagged DNA templates were immobilized on streptavidin-coated agarose beads (Smart-Lifesciences) to obtain the solid-phase templates as previously described (*25*, *26*). A detailed procedure of site1-riboCdA synthesis is described as following. In the first step, 20 μM DNA beads gently rotated with 20 μM T7 RNAP, 3.36 mM ATP, 1.28 mM guanosine 5′-triphosphate (GTP), and 128 μM cytidine 5′-triphosphate (CTP) in the initiation buffer [40 mM tris-HCl, 100 mM K_2SO_4, 6 mM $MgSO_4$, and 10 mM DTT (pH 8.0)] at 37°C for 15 min. The reaction mixture was filtered by solid-phase extraction (SPE) and washed five times by washing buffer [40 mM tris-HCl and 6 mM $MgSO_4$ (pH 8.0)]. Except noted, filtration and bead rinsing were performed between steps. In step 2, 40 μM GTP, 40 μM CTP, and 20 μM uridine 5′-triphosphate (UTP) in the elongation buffer [40 mM tris-HCl, 6 mM $MgSO_4$, and 10 mM DTT (pH 8.0)] were incubated with the solid-phase reactant at 30°C for 7 min. Subsequent steps mirrored step 2 but used different NTP mixtures as detailed in table S2. Steps 7 and 15 were conducted at a higher temperature, 37°C, to enhance yields for incorporating bulky Cy3/Cy5 into the RNA. Other fluorophore-labeled RNA samples were synthesized similarly as site1-riboCdA, except for NTP addition. Final products were purified by 12% denaturing PAGE and reversed-phase HPLC (RP-HPLC) using a C8 35-μm column (4.6 mm by 250 mm, GL Sciences, Japan). Purified RNA was exchanged to the desired buffer and stored at −80°C before use.

The labeled riboCdA samples—including AP/Cy3/Cy5-PK-riboCdA, AP/Cy3/Cy5-site1-riboCdA, AP/Cy3/Cy5-site2-riboCdA, AP/Cy3/Cy5-P1-riboCdA, AP/Cy3/Cy5-3WJ-riboCdA, and 131AP-riboCdA—were synthesized by PORDVA as previously described (*27*). DNA template and LRNA sequences used in PORDVA reactions are listed in table S6. The procedures for the six labeled samples synthesized by PORDVA are similar, except that different LRNA were used as listed table S6. The biotin-tagged DNA template used in PORDVA was immobized on the streptavidin-coated beads in the buffer [25 mM tris-HCl, 20 mM K_2SO_4, and 6 mM $MgCl_2$ (pH 8.9)] as described in the PLOR reactions. The LRNAs for the synthesis of AP/Cy3/Cy5-labeled riboCdA were synthesized by PLOR, following the procedures listed in tables S1 to S5, and the LRNA for 131AP-riboCdA was prepared by in vitro transcription. A detailed procedure of AP/Cy3/Cy5-site1-riboCdA synthesis is described as following. A total of 16 μM DNA beads gently rotated with 32 μM engineered DNA polymerase, SFM-RNAL, 130nt-site1-riboCdA, and 16 μM 2-aminopurine-5′-triphosphate (APTP) in the buffer [10 mM tris-HCl, 50 mM KCl, and 6 mM $MgCl_2$ (pH 8.9)] at 55°C for 20 min. The reaction mixture was filtered by SPE and washed five times by washing buffer [10 mM tris-HCl, 50 mM KCl, and 6 mM $MgCl_2$ (pH 8.9)] to remove residual APTP. 32 μM ATP, 64 μM GTP, 16 μM CTP, and 64 μM UTP were then incubated with the reactants at 55°C for 20 min. Subsequently, 50 U of TURBO DNase I (Invitrogen) and proteinase K (Beyotime) were added to the reaction to digest the DNA template and SFM-RNAL at 37°C for 30 min. The RNA products were purified by 12% denaturing PAGE and stored at −20°C for future use.

smFRET measurements and data analysis

Cy3Cy5-labeled riboCdA samples ranging from 50 pM to 1 nM were hybridized with a biotin-labeled oligonucleotide strand in T50 buffer [10 mM tris-HCl and 50 mM NaCl, pH 8.0) before immobilization on streptavidin-coated coverslips. After a 5-min incubation, non-immobilized RNA was removed from the chambers using the smFRET buffer [10 mM tris-HCl (pH 8.0), 50 mM NaCl, 3 mM trolox, 5 mM 3,4-dihydroxybenzoic acid, and 50 nM protocatechuate dioxygenase]. The sequence of the biotin-labeled oligonucleotide strand is listed on table S15. smFRET measurements were conducted using an objective-type total internal reflection fluorescence (TIRF) microscopy and an inverted microscope (Eclipse Ti, Nikon, Japan) at room temperature. An electron multiplying charge-coupled device (EMCCD) camera (Andor iXon Ultra 897, UK) was used to capture videos with a duration of 100 s at a frame rate of 10 Hz. Digital signals from the camera were used to modulate the excitation lasers at 532 and 640 nm (OBIS Smart Lasers, Coherent Inc., USA). The fluorescent donor, Cy3, was excited by a continuous 530-nm laser and generated by a 1.49 numerical aperture 1003 oil immersion lens for evanescent field illumination (Apo TIRF, Nikon, Japan). The open-sourced software iSMS was used to extract time-dependent signals from the single-molecule videos. Fluorescence spots on the EMCCD were fitted using a two-dimensional Gaussian function after background subtraction. The software deepFRET was used for identifying single-molecule trajectories, and manual screening may be needed to enhance data analysis accuracy. Single-molecule trajectories exhibiting anticorrelated behaviors before photobleaching were selected for following statistical analysis. The FRET efficiency, E_{FRET}, was measured using the equation: $E_{\mathrm{FRET}} = I_A/(I_A + I_D)$, where I_A and I_D denote the fluorescence intensities of the acceptor and donor, respectively. The distribution histograms of E_{FRET} were fitted with a Gaussian function based on the probability density of FRET efficiency using Origin 8.5 software. The FRET efficiency was idealized with the hidden Markov modeling (HMM) package vbFRET, which used an empirical Bayesian method to estimate the FRET states and transition time points. Transition events were determined from the states assigned by HMM and visualized through transition occupancy density plots using the Python module Matplotlib. For dynamic traces, the dwell times of each state were extracted and converted to cumulative dwell-time histograms. Lifetimes in the undocked (τ_{undock}) and docked (τ_{dock}) states were obtained by fitting the data with a single exponential function in Origin 8.5. k_{dock} and k_{undock} were calculated as the inverse of τ_{undock} and τ_{dock}, respectively.

Steady-state fluorescence spectroscopy

Steady-state fluorescence titration experiments of AP-labeled riboCdA samples interacting with c-di-AMP and Mg^{2+} were performed using a 300-nm excitation wavelength on an FLS 1000 photoluminescence spectrometer (Edinburgh Instruments Ltd., UK) at room temperature. The 0 to 200 μM c-di-AMP or 0 to 1 mM Mg^{2+} were titrated into 0.5 μM, 100 μl of 82AP-riboCdA or 103AP-riboCdA in the buffer [50 mM tris-HCl and 50 mM NaCl (pH 8.0)]. Alternatively, 0 to 100 μM c-di-AMP were titrated into 0.5 μM, 100 μl of 131AP-riboCdA samples or AP/Cy3/Cy5-labeled riboCdA samples in the buffer [50 mM tris-HCl, 50 mM NaCl, and 1 mM $MgCl_2$ (pH 8.0)]. Each measurement was repeated at least three times. The apparent dissociation constant, K_d, was determined using the Hill equation

$$\frac{F - F_0}{F_1 - F_0} = \frac{[X]^n}{\left(K_d{}^n + [X]^n\right)}$$

where F, F_0, and F_1 represent the observed, the minimum, and the maximum fluorescent intensity, respectively, and and $[X]$ represents Mg^{2+} or c-di-AMP concentration.

Probe competition assay

A 1.6 μM riboCdA, ΔP1-riboCdA, or 2bP1-riboCdA was mixed with 2 μM Cy5-labeled oligonucleotide probe (see table S15) in the buffer [50 mM tris-HCl, 110 mM KCl, and 2 mM $MgCl_2$ (pH 8.0)], heated at 85°C for 5 min, and then gradually cooled to room temperature at a rate of 5°C/min. The c-di-AMP (0 to 2000 μM) was added to the mixture and incubated at 37°C for 5 min. The reactions were then loaded to 8% native PAGE gel, visualized under a 650-nm excitation wavelength using the ChemiScope 6200 gel imager (Clinx Company, China), and quantified using the software ImageJ. Relative fluorescent intensities of Cy5 probe measured at different c-di-AMP concentrations were fitted to the Hill equation

$$\frac{F - F_0}{F_1 - F_0} = \frac{[CdA]^n}{\left(K_d{}^n + [CdA]^n\right)}$$

where F, F_0, and F_1 represent the observed, the minimum, and the maximum fluorescent intensity, respectively; [CdA] is c-di-AMP concentrations; and EC_{50} is the disassociated midpoint and n is the Hill coefficient.

C-di-AMP synthase screening

The strains containing pET28a-DisA$_{Bs}$-ON-riboCdA-GFP or pET28a-DisA$_{Bs}$ D77N-ON-riboCdA-GFP plasmids were inoculated into 1 ml of LB medium and cultured at 37°C for 12 hours. The genes of CdaA$_{Lm}$, CdaA$_{Bs}$, CdaA$_{Pt}$, CdaS$_{Bs}$, and CdaS$_{Pt}$ were purchased from Sangon and substituted for DisA$_{Bs}$ in the pET28a-DisA$_{Bs}$-ON-riboCdA-GFP construct to generate recombinant plasmids capable of expressing c-di-AMP synthases other than DisA$_{Bs}$. All plasmids were transformed into *E. coli* BL21 (DE3), and single colonies were selected for sequencing and cultured at 37°C for 12 hours. Strain growth and GFP fluorescence were measured using a Tecan Spark microplate reader with a 96-well microplate.

Construction of site-saturation mutant libraries

Nine semi-rational libraries were designed to mutate the selected residues near the binding pocket of the c-di-AMP synthases. The mutant libraries were created by overlap PCR using the parent plasmids pET28a-DisA$_{Bs}$-ON-riboCdA-GFP and pET28a-DisA$_{Bs}$-ON-2bP1-riboCdA-GFP, incorporating redundant NNK codons by Phanta Max Super-Fidelity DNA Polymerase (Vazyme, China). The primers used in PCR reactions were purchased from Sangon and are listed in table S16. Following transformation into *E. coli* BL21 (DE3), the strains were cultured on LB agar plates supplemented with kanamycin (50 mg/liter) at 37°C overnight. The single colonies exhibiting high GFP fluorescence under the ChemiScope 6200 gel imager (Clinx Company, China) were inoculated into 1 ml of LB medium containing kanamycin (50 mg/liter) and grown overnight at 37°C. A 1 μl of culture was inoculated into 200 μl of LB medium containing kanamycin (50 mg/liter) in a 96-well microplate (Corning, USA) and incubated in a microplate reader at 37°C. Fluorescence was measured every 16 min under 485-nm excitation and 509-nm emission wavelengths on a Tecan Spark microplate reader. Strains containing the parent plasmid were used as controls.

Expression and purification of c-di-AMP synthases

The genes containing DisA$_{Bs}$ (from *B. subtilis*) and its mutants were inserted into pET28a(+) between *Nde*I and *Xho*I sites using the ClonExpress II One Step Cloning Kit (Vazyme), followed by transformation into BL21 (DE3). Single colonies confirmed by sequencing were cultured overnight in 4 ml of LB medium and subsequently transferred to 100 ml of LB medium. When the optical density of 600 of the cultures reached 0.6 to 0.8, 0.5 mM isopropyl β-D-thiogalactoside was added to induce protein expression at 16°C for 16 hours. Cells were harvested by centrifugation at 12,000 rpm for 5 min, and the pellet was resuspended in the lysis buffer [50 mM tris-HCl, 300 mM NaCl, 0.1 mM EDTA, 1 mM DTT, and 0.5 mM phenylmethylsulfonyl fluoride (PMSF) (pH 7.5)]. Subsequently, the cells were sonicated, and the resulting lysate was centrifuged at 12,000 rpm for 1 hour. The supernatants were incubated with Ni-NTA agarose resin (Smart-Lifesciences, China), rinsed with the buffer [50 mM tris-HCl, 100 mM NaCl, 1 mM DTT, 0.5 mM PMSF, and 5% glycerol (pH 7.5)] to remove unbound proteins and then eluted with the buffer [50 mM tris-HCl, 100 mM NaCl, 1 mM DTT, 0.5 mM PMSF, 5% glycerol, and 300 mM imidazole (pH 7.5)]. The eluted proteins were purified using a Superdex 200 size exclusion chromatography column (GE Healthcare, USA) in the buffer [50 mM tris-HCl, 100 mM NaCl, 1 mM DTT, 0.5 mM PMSF, and 5% glycerol (pH 7.5)]. The purified proteins were then concentrated in the storage buffer [50 mM tris-HCl, 100 mM NaCl, 1 mM EDTA, and 50% glycerol (pH 7.5)] at −80°C before use.

Plasmid transformation into EcN 1917

The Ara operon, containing the PBAD promoter and AraC, was inserted into the plasmid pET28a-DisA$_{Bs}$-ON-2bP1-riboCdA-GFP, replacing the Lac operon, to obtain pBAD-DisA$_{Bs}$-ON-2bP1-riboCdA-GFP. Seven different mutants of DisA$_{Bs}$ and CdaA$_{Lm}$ (DacA) were subcloned into pBAD-DisA$_{Bs}$-ON-2bP1-riboCdA-GFP to replace DisA$_{Bs}$. Following electroporation of the plasmids into EcN 1917, transformed cells were selected as colonies on LB agar containing kanamycin (50 mg/liter). Real-time GFP measurements were performed to characterize the activity of c-di-AMP synthase mutants.

C-di-AMP synthase activity assays

The in vitro activity characterization of synthases was performed using previously described protocols[23]. A 50-μl mixture of 1 μM DisA$_{Bs}$ or mutants and 100 μM ATP was incubated in the buffer [50 mM tris-HCl, 100 mM NaCl, and 10 mM $MgCl_2$ (pH 7.5)] at 30°C for 5 to 30 min, followed by the addition of liquid nitrogen to halt the reactions. The reaction substrate (ATP) and product (c-di-AMP) were separated using RP-HPLC equipped with a C8 35-μm column (4.6 mm by 250 mm, GL Sciences, Japan) at a flow rate of 0.5 ml/min. The mobile phase consisted 90% (v/v) phosphate buffer (22.5 mM NaH_2PO_4 and 7 mM Na_2HPO_4) and 10% acetonitrile (v/v).

Statistical analysis

Statistical analysis was performed using GraphPad Prism8 and Origin 8.5 software. Quantifications shown are means ± SEM unless otherwise stated.

Supplementary Materials

This PDF file includes:
Figs. S1 to S26
Tables S1 to S16

REFERENCES AND NOTES

1. R. Corrigan, A. Gründling, Cyclic di-AMP: another second messenger enters the fray. *Nat. Rev. Microbiol.* **11**, 513–524 (2013).
2. W. Yin, X. Cai, H. Ma, L. Zhu, Y. Zhang, S. Chou, M. Galperin, J. He, A decade of research on the second messenger c-di-AMP. *FEMS Microbiol. Rev.* **44**, 701–724 (2020).
3. J. Stülke, L. Krüger, Cyclic di-AMP signaling in bacteria. *Annu. Rev. Microbiol.* **74**, 159–179 (2020).
4. K. Sureka, P. Choi, M. Precit, M. Delince, D. Pensinger, T. Huynh, A. Jurado, Y. Goo, M. Sadilek, A. Lavarone, J. Sauer, L. Tong, J. Woodward, The cyclic dinucleotide c-di-AMP is an allosteric regulator of metabolic enzyme function. *Cell* **158**, 1389–1401 (2014).
5. B. Dey, R. Dey, L. Cheung, S. Pokkali, H. Guo, J. Lee, W. Bishai, A bacterial cyclic dinucleotide activates the cytosolic surveillance pathway and mediates innate resistance to tuberculosis. *Nat. Med.* **21**, 401–406 (2015).
6. R. Dey, B. Dey, Y. Zheng, L. Cheung, J. Zhou, D. Sayre, P. Kumar, H. Guo, G. Lamichhane, H. Sintim, W. Bishai, Inhibition of innate immune cytosolic surveillance by an phosphodiesterase. *Nat. Chem. Biol.* **13**, 210–217 (2017).
7. P. Krasteva, H. Sondermann, Versatile modes of cellular regulation via cyclic dinucleotides. *Nat. Chem. Biol.* **13**, 350–359 (2017).
8. K. Parvatiyar, Z. Zhang, R. Teles, S. Ouyang, Y. Jiang, S. Iyer, S. Zaver, M. Schenk, S. Zeng, W. Zhong, Z. Liu, R. Modlin, Y. Liu, G. Cheng, The helicase DDX41 recognizes the bacterial secondary messengers cyclic di-GMP and cyclic di-AMP to activate a type I interferon immune response. *Nat. Immunol.* **13**, 1155–1161 (2012).
9. Q. Tang, M. Precit, M. Thomason, S. Blanc, F. Ahmed-Qadri, A. McFarland, D. Wolter, L. Hoffman, J. Woodward, Thymidine starvation promotes c-di-AMP-dependent inflammation during pathogenic bacterial infection. *Cell Host Microbe* **30**, 961–974.e6 (2022).
10. X. Sun, Y. Zhang, J. Li, K. Park, K. Han, X. Zhou, Y. Xu, J. Nam, J. Xu, X. Shi, L. Wei, Y. Lei, J. Moon, Amplifying STING activation by cyclic dinucleotide-manganese particles for local and systemic cancer metalloimmunotherapy. *Nat. Nanotechnol.* **16**, 1260–1270 (2021).
11. F. Wang, H. Su, D. Xu, W. Dai, W. Zhang, Z. Wang, C. Anderson, M. Zheng, R. Oh, F. Wan, H. Cui, Tumour sensitization via the extended intratumoural release of a STING agonist and camptothecin from a self-assembled hydrogel. *Nat. Biomed. Eng.* **4**, 1090–1101 (2020).
12. A. Singh, M. Praharaj, K. Lombardo, T. Yoshida, A. Matoso, A. Baras, L. Zhao, G. Srikrishna, J. Huang, P. Prasad, J. Powell, M. Kates, D. McConkey, D. Pardoll, W. Bishai, T. Bivalacqua, Re-engineered BCG overexpressing cyclic di-AMP augments trained immunity and exhibits improved efficacy against bladder cancer. *Nat. Commun.* **13**, 878 (2022).
13. D. Leventhal, A. Sokolovska, N. Li, C. Plescia, S. Kolodziej, C. Gallant, R. Christmas, J. Gao, M. James, A. Abin-Fuentes, M. Momin, C. Bergeron, A. Fisher, P. Miller, K. West, J. Lora, Immunotherapy with engineered bacteria by targeting the STING pathway for anti-tumor immunity. *Nat. Commun.* **11**, 2739 (2020).
14. N. Singh, Y. Wang, C. Wen, B. Davis, X. Wang, K. Lee, Y. Wang, High-affinity one-step aptamer selection using a non-fouling porous hydrogel. *Nat. Biotechnol.* **42**, 1224–1231 (2023).
15. K. Kavita, R. R. Breaker, Discovering riboswitches: the past and the future. *Trends Biochem. Sci.* **48**, 119–141 (2023).
16. N. White, H. Sadeeshkumar, A. Sun, N. Sudarsan, R. Breaker, Na^+ riboswitches regulate genes for diverse physiological processes in bacteria. *Nat. Chem. Biol.* **18**, 878–885 (2022).
17. L. Luo, J. Jea, Y. Wang, P. Chao, L. Yen, Control of mammalian gene expression by modulation of polyA signal cleavage at 5′ UTR. *Nat. Biotechnol.* **42**, 1454–1466 (2024).
18. A. Meyer, R. Pellaux, S. Potot, K. Becker, H. Hohmann, S. Panke, M. Held, Optimization of a whole-cell biocatalyst by employing genetically encoded product sensors inside nanolitre reactors. *Nat. Chem.* **7**, 673–678 (2015).
19. J. Nelson, N. Sudarsan, K. Furukawa, Z. Weinberg, J. Wang, R. Breaker, Riboswitches in eubacteria sense the second messenger c-di-AMP. *Nat. Chem. Biol.* **9**, 834–839 (2013).
20. A. Gao, A. Serganov, Structural insights into recognition of c-di-AMP by the riboswitch. *Nat. Chem. Biol.* **10**, 787–792 (2014).
21. C. Jones, A. Ferré-D'Amaré, Crystal structure of a c-di-AMP riboswitch reveals an internally pseudo-dimeric RNA. *EMBO J.* **33**, 2692–2703 (2014).
22. A. Ren, D. Patel, c-di-AMP binds the riboswitch in two pseudo-symmetry-related pockets. *Nat. Chem. Biol.* **10**, 780–786 (2014).
23. G. Witte, S. Hartung, K. Büttner, K. Hopfner, Structural biochemistry of a bacterial checkpoint protein reveals diadenylate cyclase activity regulated by DNA recombination intermediates. *Mol. Cell* **30**, 167–178 (2008).
24. Y. Oppenheimer-Shaanan, E. Wexselblatt, J. Katzhendler, E. Yavin, S. Ben-Yehuda, c-di-AMP reports DNA integrity during sporulation in *Bacillus subtilis*. *EMBO Rep.* **12**, 594–601 (2011).
25. Y. Liu, E. Holmstrom, J. Zhang, P. Yu, J. Wang, M. Dyba, D. Chen, J. Ying, S. Lockett, D. Nesbitt, A. Ferré-D'Amaré, R. Sousa, J. Stagno, Y. Wang, Synthesis and applications of RNAs with position-selective labelling and mosaic composition. *Nature* **522**, 368–372 (2015).
26. Y. Liu, E. Holmstrom, P. Yu, K. Tan, X. Zuo, D. Nesbitt, R. Sousa, J. Stagno, Y. Wang, Incorporation of isotopic, fluorescent, and heavy-atom-modified nucleotides into RNAs by position-selective labeling of RNA. *Nat. Protoc.* **13**, 987–1005 (2018).
27. D. Chen, Z. Han, X. Liang, Y. Liu, Engineering a DNA polymerase for modifying large RNA at specific positions. *Nat. Chem.* **17**, 382–392 (2025).
28. D. Kalia, G. Merey, S. Nakayama, Y. Zheng, J. Zhou, Y. Luo, M. Guo, B. Roembke, H. Sintim, Nucleotide, c-di-GMP, c-di-AMP, cGMP, cAMP, (p)ppGpp signaling in bacteria and implications in pathogenesis. *Chem. Soc. Rev.* **42**, 305–341 (2013).
29. Y. Jiang, X. Li, F. Qian, B. Sun, X. Wang, Y. Zhang, D. Zhang, M. Geng, Z. Xie, S. Yang, Fine-tuning bacterial cyclic di-AMP production for durable antitumor effects through the activation of the STING pathway. *Research* **6**, 0102 (2023).
30. S. Kwon, H. Ngo, J. Son, Y. Hong, J. Min, Exploiting bacteria for cancer immunotherapy. *Nat. Rev. Clin. Oncol.* **21**, 569–589 (2024).
31. J. Luke, S. Piha-Paul, T. Medina, C. Verschraegen, M. Varterasian, A. Brennan, R. Riese, A. Sokolovska, J. Strauss, D. Hava, F. Janku, Phase I study of SYNB1891, an engineered *E. coli* Nissle strain expressing STING agonist, with and without atezolizumab in advanced malignancies. *Clin. Cancer Res.* **29**, 2435–2444 (2023).
32. K. Suddala, J. Yoo, L. Fan, X. Zuo, Y. Wang, H. Chung, J. Zhang, Direct observation of tRNA-chaperoned folding of a dynamic mRNA ensemble. *Nat. Commun.* **14**, 5438 (2023).
33. X. Niu, Z. Xu, Y. Zhang, X. Zuo, C. Chen, X. Fang, Structural and dynamic mechanisms for coupled folding and tRNA recognition of a translational T-box riboswitch. *Nat. Commun.* **14**, 7394 (2023).
34. A. Haller, U. Rieder, M. Aigner, S. Blanchard, R. Micura, Conformational capture of the SAM-II riboswitch. *Nat. Chem. Biol.* **7**, 393–400 (2011).
35. C. Jones, A. Ferré-D'Amaré, Long-range interactions in riboswitch control of gene expression. *Annu. Rev. Biophys.* **46**, 455–481 (2017).
36. S. Parmar, D. Bume, C. Connelly, R. Boer, P. Prestwood, Z. Wang, H. Labuhn, K. Sinnadurai, A. Feri, J. Ouellet, P. Homan, T. Numata, J. Schneekloth, Mechanistic analysis of riboswitch ligand interactions provides insights into pharmacological control over gene expression. *Nat. Commun.* **15**, 8173 (2024).
37. J. Wickiser, W. Winkler, R. Breaker, D. Crothers, The speed of RNA transcription and metabolite binding kinetics operate an FMN riboswitch. *Mol. Cell* **18**, 49–60 (2005).
38. S. Ray, A. Chauvier, N. Walter, Kinetics coming into focus: single-molecule microscopy of riboswitch dynamics. *RNA Biol.* **16**, 1077–1085 (2019).
39. E. Strobel, L. Cheng, K. Berman, P. Carlson, J. Lucks, A ligand-gated strand displacement mechanism for ZTP riboswitch transcription control. *Nat. Chem. Biol.* **15**, 1067–1076 (2019).

40. M. Boyd, W. Thavarajah, J. Lucks, N. Kamat, Robust and tunable performance of a cell-free biosensor encapsulated in lipid vesicles. *Sci. Adv.* **9**, eadd6605 (2023).
41. F. Isaacs, D. Dwyer, J. Collins, RNA synthetic biology. *Nat. Biotechnol.* **24**, 545–554 (2006).
42. P. Q. Nguyen, L. R. Soenksen, N. M. Donghia, N. M. Angenent-Mari, H. de Puig, A. Huang, R. Lee, S. Slomovic, T. Galbersanini, G. Lansberry, H. M. Sallum, E. M. Zhao, J. B. Niemi, J. J. Collins, Wearable materials with embedded synthetic biology sensors for biomolecule detection. *Nat. Biotechnol.* **39**, 1366–1374 (2021).
43. E. M. Zhao, A. S. Mao, H. de Puig, K. Zhang, N. D. Tippens, X. Tan, F. A. Ran, I. Han, P. Q. Nguyen, E. J. Chory, T. Y. Hua, P. Ramesh, D. B. Thompson, C. Y. Oh, E. S. Zigon, M. A. English, J. J. Collins, RNA-responsive elements for eukaryotic translational control. *Nat. Biotechnol.* **40**, 539–545 (2022).
44. Y. Xue, J. Li, D. Chen, X. Zhao, L. Hong, Y. Liu, Observation of structural switch in nascent SAM-VI riboswitch during transcription at single-nucleotide and single-molecule resolution. *Nat. Commun.* **14**, 2320 (2023).
45. K. Watters, E. Strobel, A. Yu, J. Lis, J. Lucks, Cotranscriptional folding of a riboswitch at nucleotide resolution. *Nat. Struct. Mol. Biol.* **23**, 1124–1131 (2016).
46. Y. Li, A. Arce, T. Lucci, R. Rasmussen, J. Lucks, Dynamic RNA synthetic biology: new principles, practices and potential. *RNA Biol.* **20**, 817–829 (2023).

Acknowledgments: We thank the Student Innovation Center at Shanghai Jiao Tong University for assistance in smFRET data collection. **Funding:** This work was supported by the National Natural Science Foundation of China (grant 32471342 to Y.L.) and the National Key Research and Development Program of China (grant 2021YFA0910300 to Y.L.). **Author contributions:** Conceptualization: D.C., L.H., and J.L. Resources: D.C. and J.L. Methodology: D.C., J.L., Y.W., and L.H. Investigation: D.C., J.L., and Y.W. Visualization: D.C. and J.L. Data curation: D.C. and J.L. Validation: D.C. and Y.W. Formal analysis: D.C. and J.L. Supervision: J.L., L.H., and Y.L. Writing—original draft: D.C., J.L., Y.W., and Y.L. Writing—review and editing: D.C., J.L., and Y.L. Funding acquisition: Y.L. Software: D.C. and J.L. Project administration: J.L. and Y.L. **Competing interests:** The authors declare that they have no competing interests. **Data and materials availability:** All data needed to evaluate the conclusions in the paper are present in the paper and/or the Supplementary Materials.

Submitted 11 October 2024
Accepted 26 February 2025
Published 2 April 2025
10.1126/sciadv.adt8165